

Removal of deposited metal particles on a horizontal surface by vertical submerged impinging jets

Han Peng¹, Xinliang Jia^{2,3}, Xiaofang Guo^{2,3}, Yubo Jiang^{2,3}, Zhipeng Li^{1,*}, Zhengming Gao^{1,*},
and J. J. Derksen⁴.

¹ State Key Laboratory of Chemical Resource Engineering, School of Chemical Engineering,
Beijing University of Chemical Technology, Beijing 100029, China

² China Nuclear Power Engineering Co., Ltd., Beijing 100840, China

³ Innovation Center for Nuclear Facilities Decommissioning and Radioactive Waste
Management Technology, Beijing 100840, China

⁴ School of Engineering, University of Aberdeen, Aberdeen AB24 3UE, UK.

Abstract: Jet is known as a maintenance-free stirring technique for nuclear wastewater treatment and demonstrates great potential in transport of radioactive particles. Removal processes of horizontal sediment beds driven by impinging jets were experimentally investigated using image capture and processing technique. The beds were composed of heavy fine particles with particle density ranging from 3700 to 12600 kg·m⁻³ and particle diameter from 5 to 100 μm. The jet Reynolds number varied between 4300 and 9600. The single-phase large eddy simulation method was used for calculating both jet flow characteristics and wall shear stresses. The effects

19 of jet strength, particle density, particle diameter, and bed thickness on bed mobility in terms of
20 the critical Shields numbers were considered. Specifically, the critical Shields number was found
21 to be intricately related to properties of particles, and independent of jet intensity. A new Shields
22 number curve for stainless-steel particles was found, and a model was proposed to predict the
23 transport rate of thin beds, with $R^2 = 0.963$.

24

25 **KEYWORDS:** Particle removal; Impinging jet; Shields number; Computational fluid dynamics,
26 CFD; Two-phase flow; Transport.

27

28 * Corresponding author: Zhipeng Li, Zhengming Gao.

29 E-mail addresses: lizp@mail.buct.edu.cn (Z. Li), gaozm@mail.buct.edu.cn (Z. Gao).

30

31 **Highlights:**

- 32 1. Particle removal processes by jets were investigated experimentally.
- 33 2. Effects of jet and particle on critical Shields number were discussed.
- 34 3. A model for predicting the initial transport rate of thin beds was proposed.
- 35 4. Wall shear stresses are accurately predicted using large eddy simulation.

36

37

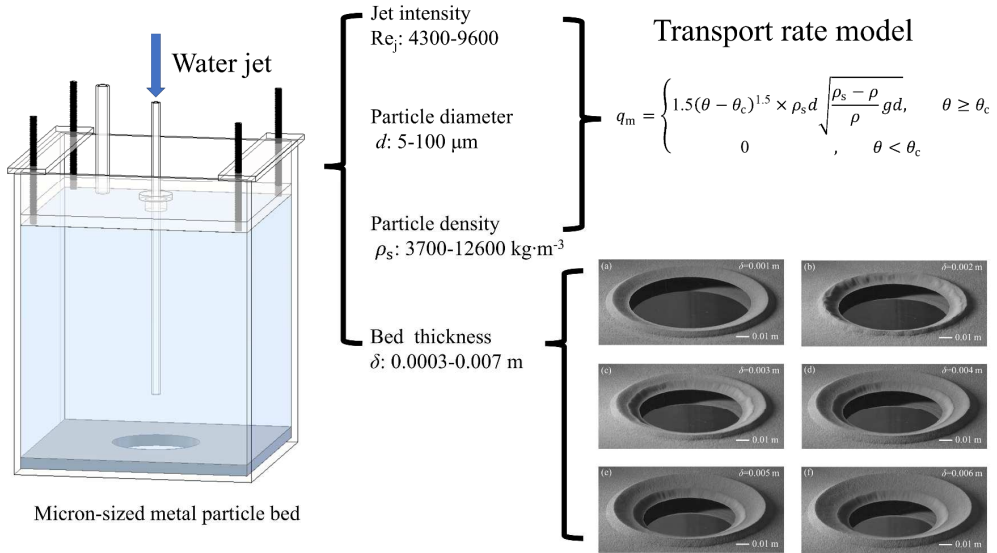
38

39

40

41

42 **Graphical abstract:**



43

44

45 **1. Introduction.**

46 Jet agitators are widely applied for solids suspension processes in large nuclear waste storage
47 tanks [1-3]. Generally, the radioactive particles are too heavy to be uniformly suspended in tanks.
48 The key to design these jet agitators lies in predicting the cleaning efficiency of the jet on the
49 bottom wall. For noncohesive particles, their motion is mainly determined by the competition
50 between the shear stress of liquid flow and the net weight of particles. This competition is
51 reflected in the dimensionless Shields number [4]: $\theta \equiv \frac{\tau}{g(\rho_s - \rho)d}$, where τ is the shear stress at the
52 bed surface, g is the gravitational acceleration, ρ_s is the particle density, ρ is the liquid density,
53 and d is the average particle size. Further, the critical Shields number [5] is used to predict the
54 incipient bed motion: $\theta_c \equiv \frac{\tau_c}{g(\rho_s - \rho)d}$, where τ_c is the critical shear stress. That is, the critical
55 Shields number reflects the ease with which particle motion is initiated. When the Shields
56 number reaches its critical value, particles begin to exhibit initial motion. This provides a
57 quantitative basis for predicting key phenomena such as particle transport initiation and bed layer
58 changes. Other dimensionless groups also play significant roles in the cleaning process. The jet
59 Reynolds number Re_j quantifies the velocity of jet, and the particle Reynolds number Re_p
60 reflects the ratio of the inertia force to the viscous force acting on particles.

61 Extensive experimental studies on cleaning efficiency of jets have been reported. Young et al.
62 [6] measured the wall shear stress exerted by impinging jets and proposed a correlation between
63 wall shear stress and removal of sparsely distributed particles. Wilson et al. [7] got a simple
64 function between the cleaning radius of jets and time. Wall shear stress is an important parameter
65 for calculating the driving force of particles, but experimental measurement of the wall shear
66 stress exerted by impinging jets is challenging. An optical method such as particle image
67 velocimetry (PIV), is incompetent to resolve the near-wall shear flows due to the limits on spatial

68 resolution [8]. Phares et al. [9] proposed that the electrochemical method exhibited the highest
69 accuracy among the common indirect methods for measuring the wall shear stress.
70 Electrochemical diffusion techniques have been employed in recent studies exploring the
71 characteristic of impinging jet flow [10-12].

72 Apart from experimental techniques, computational fluid dynamics (CFD) simulations offer an
73 alternative means of obtaining wall shear stresses. Eisner [13] used CFD simulations to calculate
74 the wall shear stresses exerted by impinging jets, and the results of an unpaired, two-tailed t-test
75 (with a significance level of $P < 0.05$) indicated no statistically significant difference between
76 simulated and experimental data.

77 In this study, an experimental setup for submerged impinging jets was established. The first
78 aim of this study is to validate the CFD simulations for predicting the single-phase impinging jet
79 flow characteristics. It is achieved by comparing the simulated velocities and wall shear stresses
80 with those reported in the literature. The second aim is to identify the key factors influencing the
81 removal process of sediment bed under impinging jets. A series of heavy particles made of
82 metals with densities larger than $8000 \text{ kg}\cdot\text{m}^{-3}$ were used to form beds, which has not been
83 reported before.

84 The rest of this study is organized as follows. The parameters of the flow system are detailed in
85 Section 2, including jet flow rates and properties of particles. Then in next section, the CFD
86 methodology is summarized, and the simulations are verified. In the results section (Section 4),
87 we show the effects of jet intensity, particle density, particle diameter and bed thickness on the
88 removal processes. Along with a corrected coefficient, the model proposed in this study is valid
89 for the prediction of transport rates of thin beds. The last section summarizes the key findings of
90 this study and discusses the direction of future research.

91

92 **2. Experimental setup**

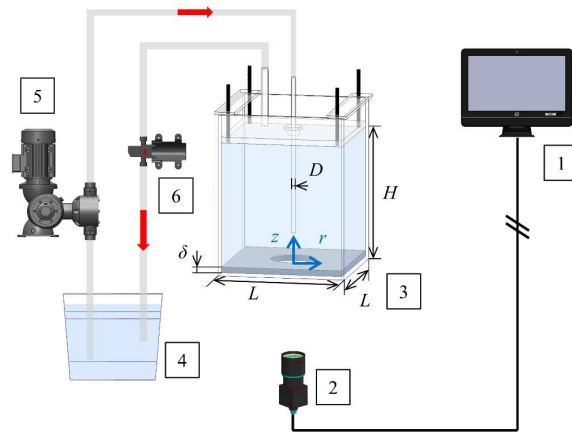
93 **2.1 Flow system.**

94 The jet flow configuration is sketched in Fig. 1. A square glass tank is used with a side length
95 L of 0.22 m and a liquid height H of 0.23 m. The jets are from a smooth glass circular tube with
96 an inner diameter D of 0.005 m, an outer diameter D_o of 0.008 m, and a length of 0.3 m. The
97 distance from tube outlet to bottom wall is constant and equal to 0.05 m. Deionized water fills
98 the tank. Its temperature is maintained at $20 \pm 1^\circ\text{C}$, with an estimated density ρ of $1000 \text{ kg}\cdot\text{m}^{-3}$
99 and a dynamic viscosity μ of $0.001 \text{ kg}\cdot\text{m}^{-1}\cdot\text{s}^{-1}$.

100 The characteristics of jets are determined by their jet Reynolds numbers $\text{Re}_j = \frac{\rho u_0 D}{\mu}$, where u_0
101 is the mean flow velocity within the tube. The Reynolds numbers Re_j varies between 4260, 6530,
102 and 9570, corresponding to flow rates of 60, 92.6, and 135 $\text{L}\cdot\text{h}^{-1}$, respectively. The flow rates
103 were measured by weighing the mass of outlet liquid per unit time, with error within $\pm 1\%$.

104 A LCA1-M910S metering pump (LEWA, Germany) provided stable jet flows, with flow
105 fluctuations less than $\pm 3\%$. The circulating pump 6 in Fig. 1 kept the constant liquid height. To
106 record the temporal evolutions of the cleaned areas, a GO-5000M-USB camera (JAI, Denmark),
107 of $2592 \times 1944 \text{ pixels}^2$ resolution with pixel size of $66 \times 66 \mu\text{m}^2$, was placed below the glass
108 tank, as shown in Fig. 1. Considering lens distortion, the error in size measurement was kept
109 within $\pm 0.5\%$.

110 Before each experiment, a particle bed with an initial thickness δ ranging from 0.0003 to 0.007
111 m was uniformly spread on the bottom wall by using a special scraper. The metering pump 5 and
112 circulating pump 6 were started sequentially, as shown in Fig. 1. Under the action of jet, a
113 cleaned area appeared, and the evolution of its radius over time was recorded by camera 2.



114

115 **Fig. 1.** Experimental setup: 1. computer, 2. camera, 3. jet system, 4. water storage tank, 5.

116 metering pump, 6. circulating pump.

117

118 2.2 Particle properties.

119 The six kinds of particles used to form the beds in the experiments are listed in Table 1. The
 120 particle density ρ_s ranges from 3700 to 12600 $\text{kg}\cdot\text{m}^{-3}$, and the particle diameter d ranges from 5

121 to 100 μm . The particle densities were measured by hydrostatic weighing method, with error
 122 within $\pm 1\%$. Among the particles, those with a diameter of 5 μm exhibit irregular shapes due to

123 manufacture limitations, while the other particles are approximately spherical, with some of them
 124 shown in Fig. 2. The dimensionless submerged specific weight of sediment s is defined as

125 $\rho_s/\rho - 1$.

126

127

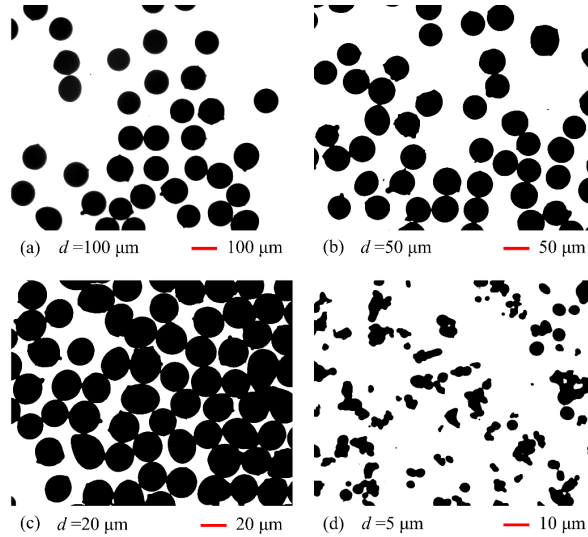
Table 1. Properties of particles used in the experiments

Material	Diameter (μm)	s	Shape
Aluminum oxide	100 ± 5	2.70	Spherical
Stainless steel	5 (average)	7.04	Irregular
Stainless steel	20 ± 5	7.04	Spherical

128

Stainless steel	50 ± 5	7.04	Spherical
Stainless steel	100 ± 5	7.04	Spherical
Tungsten carbide	100 ± 5	11.6	Spherical

129



130 **Fig. 2.** Morphology of stainless-steel particles with average diameter of (a) 100 μm; (b) 50 μm;
131 (c) 20 μm; (d) 5 μm, as captured by a MIT1818072 metallographic microscope (CNOPTEC,
132 China).

133

134 3. Numerical methods and validation

135 In this section, we show the large eddy simulation (LES) method for predicting the single-
136 phase jet flow first, and then we validate the simulations by using the experimental data on
137 velocities and wall shear strain rates from the literature [12].

138 3.1 Large eddy simulation.

139 The fundamental equations guiding LES for incompressible fluids are the Navier-Stokes
140 equations and continuity equations, both of which have undergone filtering.

141
$$\frac{\partial \bar{u}_i}{\partial t} + \frac{\partial \bar{u}_i \bar{u}_j}{\partial x_j} = -\frac{1}{\rho} \frac{\partial \bar{p}}{\partial x_i} + \nu \frac{\partial^2 \bar{u}_i}{\partial x_j \partial x_j} - \frac{\partial \sigma_{ij}}{\partial x_j} \quad (1)$$

142
$$\frac{\partial \bar{u}_i}{\partial x_i} = 0 \quad (2)$$

143 where u is the velocity component, i and j are the coordinate directions, t is the time, p is the
 144 pressure, ν is the kinematic viscosity, σ is the sub-grid scale stress tensor, and the overbars
 145 denote the filtered variable on resolved scales.

146 After filtering by the resolved scale grid, the effect of filtering is represented by the sub-grid
 147 scale stress tensor

148
$$\sigma_{ij} = \overline{u_i u_j} - \bar{u}_i \bar{u}_j \quad (3)$$

149 Based on the eddy-viscosity assumption in most sub-grid scale models, the sub-grid scale
 150 stress tensor is modelled as

151
$$\sigma_{ij} - \frac{1}{3} \delta_{ij} \sigma_{kk} = -2\nu_t \bar{S}_{ij} \quad (4)$$

152 where δ_{ij} is the Kronecker delta, ν_t is the eddy viscosity, and the deformation tensor of the
 153 resolved field is

154
$$\bar{S}_{ij} = \frac{1}{2} \left(\frac{\partial \bar{u}_i}{\partial x_j} + \frac{\partial \bar{u}_j}{\partial x_i} \right) \quad (5)$$

155 The wall-adapting local eddy-viscosity (WALE) model [14] is designed to predict near-wall
 156 flow characteristics and correctly handle the laminar-to-turbulent transition processes. The model
 157 produces zero eddy viscosity in the vicinity of a wall so that no damping function is needed to
 158 compute wall bounded flows. Moreover, the high-resolution requirements for wall boundary
 159 layers result in the WALE model being recommended only when near-wall flows are important
 160 [15]. The eddy viscosity is modeled by

161
$$\nu_t = (\min(\kappa y, C_w \Delta))^2 \frac{(s_{ij}^d s_{ij}^d)^{3/2}}{(\bar{s}_{ij} \bar{s}_{ij})^{5/2} + (s_{ij}^d s_{ij}^d)^{5/4}} \quad (6)$$

162
$$S_{ij}^d = \frac{1}{2}(\bar{g}_{ij}^2 + \bar{g}_{ji}^2) - \frac{1}{3}\delta_{ij}\bar{g}_{kk}^2, \bar{g}_{ij} = \frac{\partial \bar{u}_i}{\partial x_j} \quad (7)$$

163 where $\kappa = 0.41$ is the von Karman constant, y is the distance to the closest wall, $C_w = 0.325$ is a
 164 coefficient, $\Delta = V^{1/3}$ is the filter width, V is the cell volume, and S_{ij}^d is the traceless symmetric
 165 part of the square of the velocity gradient tensor.

166 All parameters and operating conditions in the simulations are set as they are in the
 167 experiments. A uniform velocity inlet is located at the top of the tube, and a uniform pressure
 168 outlet is situated on the top surface of the tank. The wall boundary condition is set as no-slip.

169 Structured, nonuniformly distributed hexahedral grids are used. Although the WALE model is
 170 a y^+ -insensitive wall treatment model [14], we set up the boundary layer grids on both tube inner
 171 wall and tank bottom wall. The dimensionless wall distance $y^+ \equiv \frac{\rho y U_f}{\mu}$ remains around 1 for the
 172 cell closest to the wall, $U_f = \sqrt{\tau/\rho}$ is the friction velocity, and τ is the wall shear stress. In fact,
 173 we cannot know the value of y^+ except from the simulation results. If y^+ is greater than
 174 expected, a new and finer boundary layer grid is required.

175 The Courant-Friedrichs-Lewy (CFL) number serves as a criterion for assessing the stability of
 176 simulations, and is defined as $\frac{u\Delta t}{\Delta x}$, where the Δt is time step of the simulation, Δx is the grid
 177 spacing. With maximum grid spacing $\Delta x_{\max} \leq 0.0004$ m and $\text{CFL} \leq 2.0$, the simulated results in
 178 Section 4 are grid independent, see Fig. S1 in the supplementary data. These criteria are used for
 179 all the simulations. Data sampling begins when the average pressure on the sidewall of the tank
 180 is stable. The total sampling time for each simulation is 5 seconds, during which time the jet
 181 traverses the study area ($r/D \leq 15$) at least 20 times.

182 The ANSYS Fluent 2022R1 software [15] is used to simulate the jet flow. The coupling
 183 between pressure and velocity is accomplished by the semi-implicit method for pressure linked

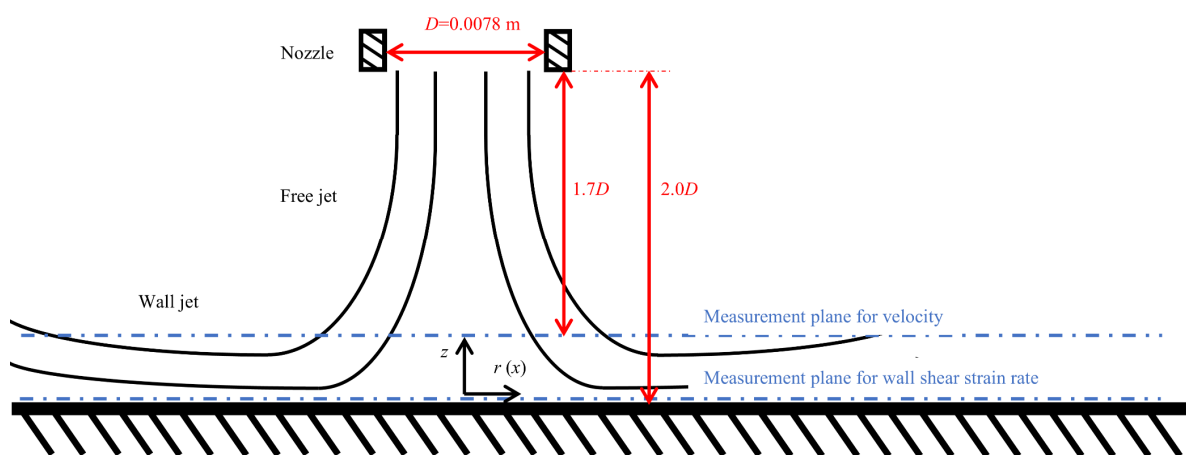
184 equations. For the spatial discretization of the momentum equations, the central differencing
185 scheme is employed, while the second-order implicit scheme is utilized for the transient
186 formulation.

187

188 3.2 Simulation validation.

189 To support the validity of simulations in this study, we cited extensive data from the literature
190 [12] on velocities and wall shear strain rates of jets from three round orifice nozzles. The
191 impinging jet and the measurement plane are schematically shown in Fig. 3a. The velocity
192 profiles at $z/D = 0.3$ and wall shear strain rate profiles at $z/D = 0$ were measured by using PIV
193 and electrochemical diffusion technique, respectively.

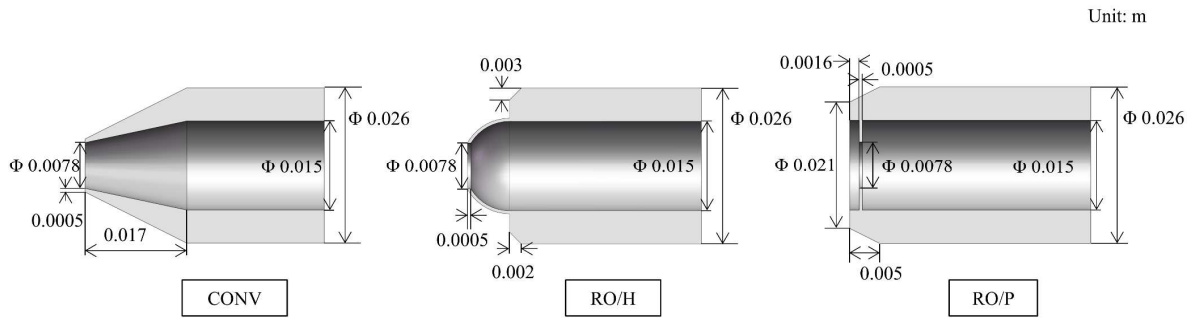
194 Fig. 3b displays a schematic diagram of three nozzles used. The numerical model and details
195 are the same as those in Section 3.1. Three dimensional geometric parameters and operation
196 conditions in the simulations are set as they are in the literature [12], with a jet Reynolds number
197 Re_j of 5620. We started the simulations from stationary status and began to collect time-averaged
198 velocity field when the jet stabilized.



199

200

(a)



201

202

(b)

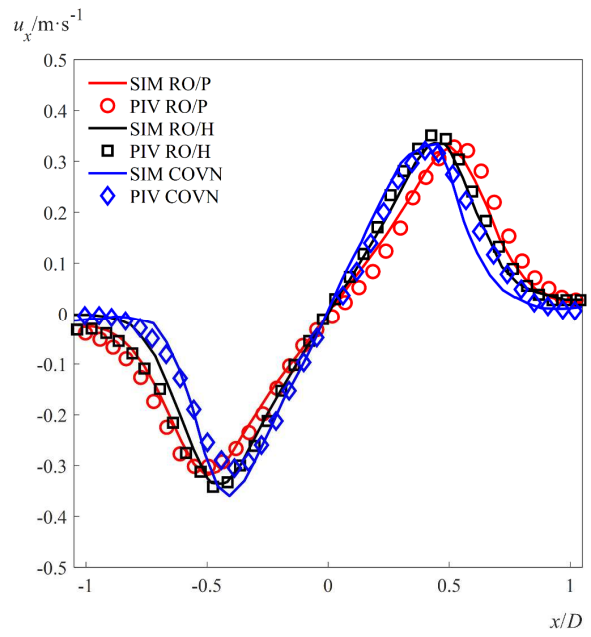
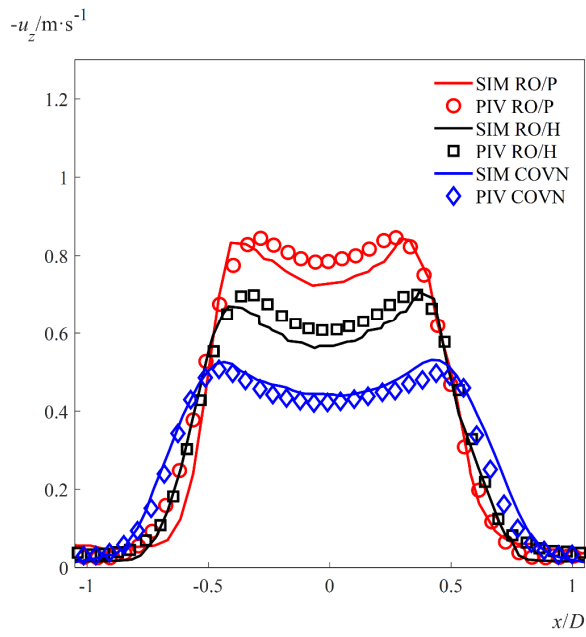
203 **Fig. 3.** Schematic description of (a) impinging jet and (b) three nozzles: convergent nozzle
 204 (CONV), round orifice on hemisphere (RO/H), and round orifice on plate (RO/P). [12]

205

206 The profiles of simulated and experimental streamwise velocity u_z are given in Fig. 4a, and
 207 they all exhibit M shapes. Sodjavi et al. [12] attributed this flow deceleration in the core region
 208 to the high static pressure at the impact point ($x/D = 0, z/D = 0$). [12] Simulations yield results
 209 close to experimental values when predicting transverse velocity u_x , as shown in Fig. 4b. Given
 210 that the maximum deviation at the core of jets is less than 8% in both figures, the simulated
 211 results match well with the experimental data.

212 Besides the velocity, the profiles of wall shear strain rate $\gamma = \tau/\mu$ are given in Fig. 4c, which
 213 are obtained by using three nozzles. Along the direction away from the impact point, the shear
 214 strain rates decrease after reaching the peak values. The simulated wall shear strain rates are
 215 within $\pm 9\%$ of the ones measured. The accuracy of WALE LES model in calculating impinging
 216 jet flow field has been confirmed. Compared with the WALE LES model, three Reynolds
 217 Averaged Navier-Stokes (RANS) turbulence models all overestimate the wall shear strain rates
 218 when $r/D > 1.5$, as shown in Fig. 4d.

219

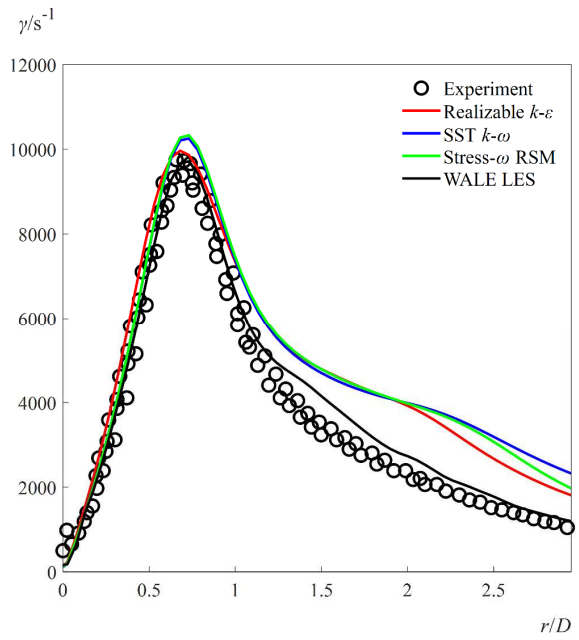
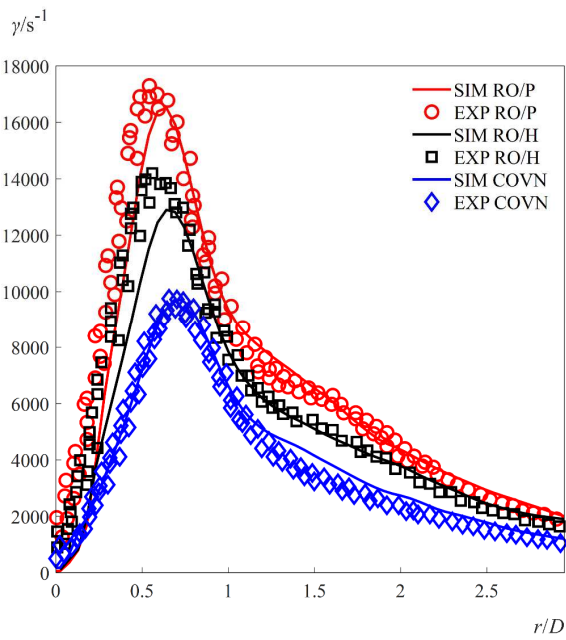


220

221

(a)

(b)



222

223

(c)

(d)

224 **Fig. 4.** Velocity profiles ($z/D = 0.3$) obtained by LES and PIV along the (a) streamwise
225 direction, and (b) transverse direction. Wall shear strain rate profiles ($z/D = 0$) obtained by LES
226 and electrochemical diffusion technique (c) by using the three nozzles as shown in Fig. 3b, and
227 (d) by simulations with four models for the COVN nozzle.

228

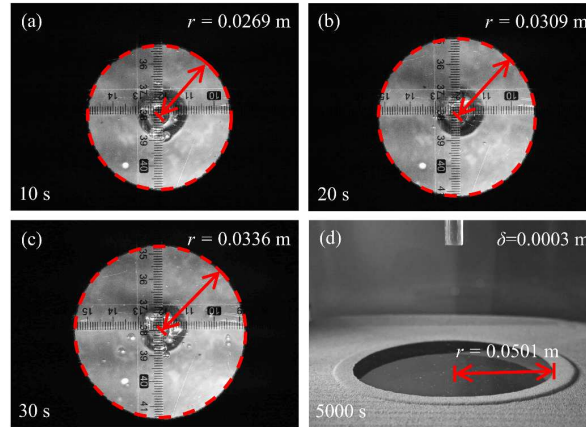
229 **4. Results and discussion**

230 **4.1 Interaction process between jets and particles.**

231 Based on our visual observations, the impinging jet swept particles from the center into the
232 surrounding region. The photographs of the particle bed, captured by the camera below the
233 bottom wall at the time points when the jet lasted for 10 s, 20 s, and 30 s, are presented in Fig. 5.
234 By image processing using the circle Hough transform [16] method, we recognize and record the
235 cleaned areas as dashed lines shown in Fig. 5. There is no particle inside the red circles, and the
236 radii of circles are called the removal radii.

237 Fig. 5d shows a steady bed, with its radius considered as the critical removal radius. To ensure
238 that the beds reach a stable state, the duration of the jets must be sufficiently long. We selected a
239 working time of 5000 seconds, balancing the accuracy against the time cost of experiments,
240 given that the differences between radii at 4000 seconds and 5000 seconds were less than 3% for
241 all beds considered.

242



243

244 **Fig. 5.** Photographs of beds from the bottom view at (a) 10 s; (b) 20 s; (c) 30 s. (d) Photograph of
 245 steady bed from the side view at 5000 s. ($Re_j = 6530$, $s = 7.04$, $d = 100 \mu\text{m}$, $\delta = 0.0003 \text{ m}$)

246

247 **4.2 Effect of jet intensity.**

248 In this section, we will discuss the effect of jet intensity on the critical Shields numbers of
 249 particles, starting with a description of the jet flow field.

250 With the diameter of the tube outlet as the characteristic size, the jet Reynolds numbers were
 251 set to 4260, 6530, and 9570. The profiles of dimensionless velocity u_z/u_0 at distance from the
 252 wall $z/D = 0.25$ and $z/D = 9.75$ are shown in Fig. 6a. The profiles are nearly identical beyond
 253 the core region ($r/D < 0.5$) at different jet Reynolds numbers, which reveals the similarity in
 254 flow characteristics.

255 Shear stress is a significant driving force for the motion of non-cohesive particles in the shear
 256 flow [17]. Given that there were no particles in the cleaned area and only a few at the removal
 257 radius (see the base of dune in Fig. 5d), the wall shear stress from single-phase LES simulation is
 258 a good estimate of the shear stress on particles at the removal radius. The profiles of wall shear
 259 strain rates obtained by using the LES method are shown in Fig. 6b, and some bumps are noticed
 260 around $r/D = 2$. Meslem et al. [18] reviewed relevant studies and found that the curves of wall

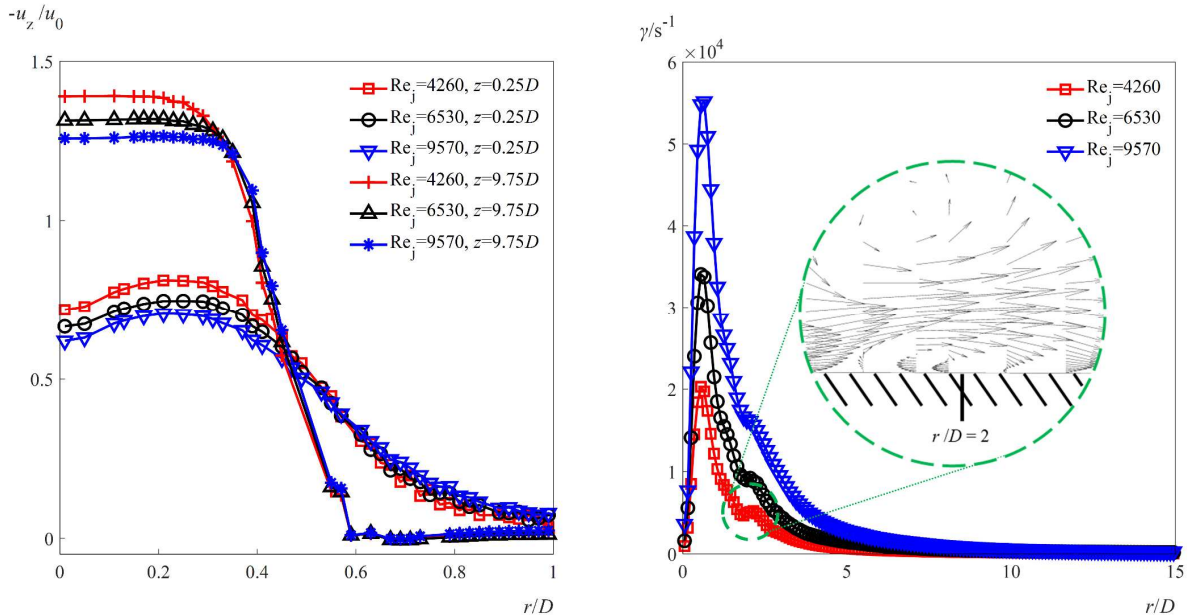
261 shear strain rates were smooth when $Re_j < 2000$. Tummers et al. [19] attributed these bumps to
 262 flow reversal. We plot the flow field near the wall at the position of the green dashed line when
 263 $Re_j = 4260$, and confirm the existence of flow reversal.

264 The temporal evolutions of bed removal radii r in experiments are given in Fig. 6c. Beds
 265 moved fast near the impact point and then gradually stabilized. The critical removal radii of beds
 266 are recorded at $t = 5000$ s, and are positively correlated with the jet Reynolds numbers.

267 Fig. 6d is a partial enlargement of Fig. 6b. Taking the three r/D positions of critical removal
 268 radii in Fig. 6c as horizontal coordinates, we mark the three critical shear strain rates
 269 corresponding to three jet Reynolds numbers with green dashed lines, and find that they are each
 270 approximately 350 /s. The critical Shields number can be calculated using the equation $\theta_c =$

271
$$\frac{\tau_c}{g(\rho_s - \rho)d} = \frac{\mu\gamma_c}{g(\rho_s - \rho)d} \approx 0.0509$$
, which is in agreement with the critical Shields number of 0.05 for

272 sand on a horizontal bed estimated by Fredsøe et al. [20]. It means that the jet intensity has very
 273 little effect on the critical Shields number.

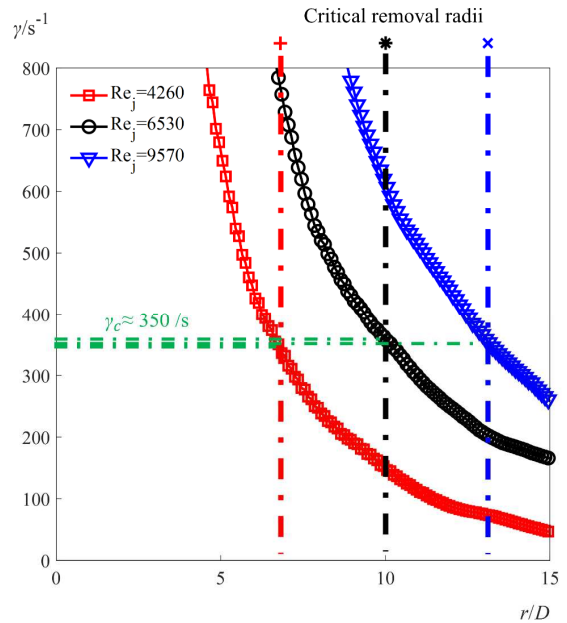
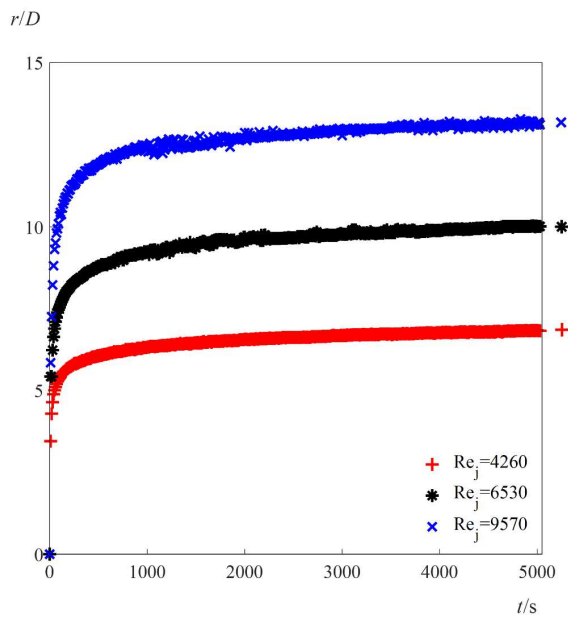


274

275

(a)

(b)



276

277

(c)

(d)

278 **Fig. 6.** (a) Simulated velocity profiles at $z/D = 0.25$ and $z/D = 9.75$; (b) simulated wall shear
 279 strain rate profiles; (c) experimental bed removal radii as a function of time for different Re_j ; (d)
 280 estimation method of critical shear strain rates. ($s = 7.04$, $d = 100 \mu\text{m}$, $\delta = 0.0003 \text{ m}$).

281

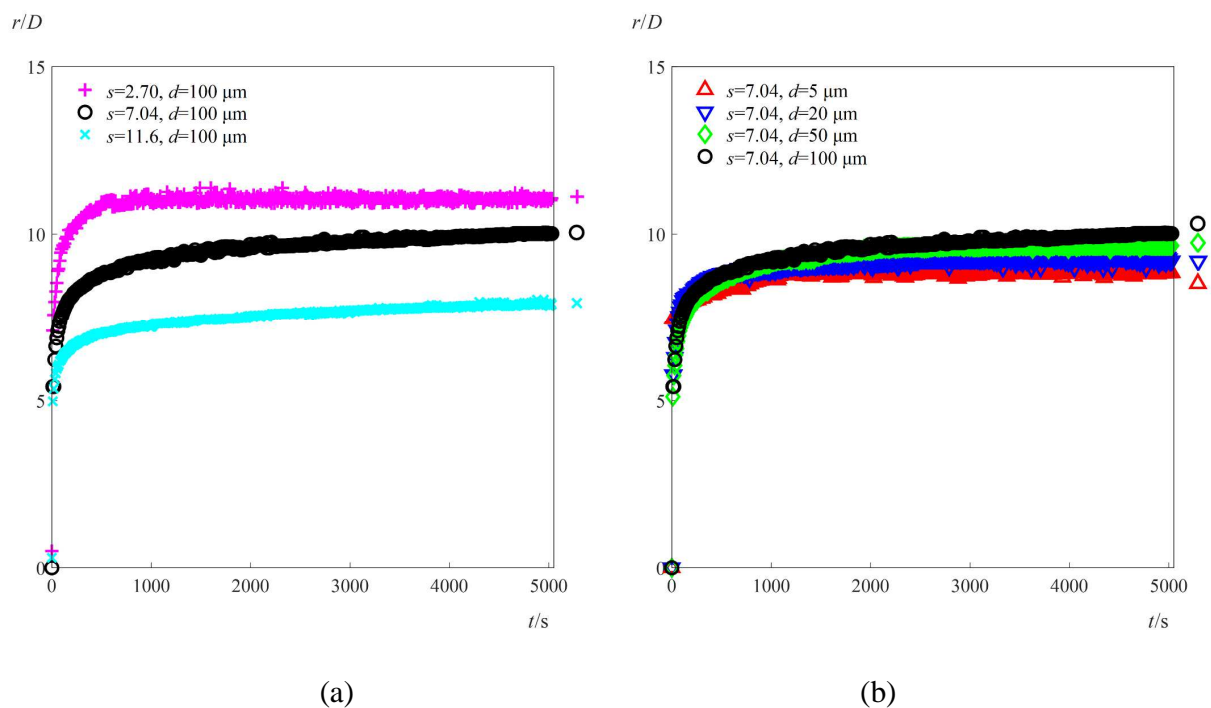
282 4.3 Effect of particle property.

283 Three materials were selected for the particles, namely alumina ($s = 2.70$), stainless steel
 284 ($s = 7.04$), and tungsten carbide ($s = 11.6$). With a jet Reynolds number of 6530, an average
 285 particle diameter of $100 \mu\text{m}$, and an initial bed thickness of 0.0003 m , the temporal evolutions of
 286 bed removal radii in the experiments are presented in Fig. 7a. As the particle densities increase,
 287 the critical removal radii of beds decrease.

288 The particle diameter is another variable when calculating the Shields number. Four kinds of
 289 stainless-steel particles were selected as the research objects, and their average diameters were 5,

290 20, 50, and 100 μm , respectively. With an initial bed thickness of 0.0003 m and a jet Reynolds
 291 number of 6530, the experimental results are shown in Fig. 7b. In comparison with particle
 292 density, the diameter of particle has less effect on the critical removal radius.

293 It is interesting to note that smaller density and smaller diameter shorten the time the beds take
 294 to reach stability in Fig. 7. This might be that their smaller inertia enables the particles to respond
 295 more rapidly to shear stresses, especially those stresses slightly above the critical shear stresses.



296
 297 (a) (b)
 298 **Fig. 7.** Bed removal radii as a function of time for different (a) particle density, and (b) particle
 299 diameter. ($\text{Re}_j = 6530, \delta = 0.0003 \text{ m}$)

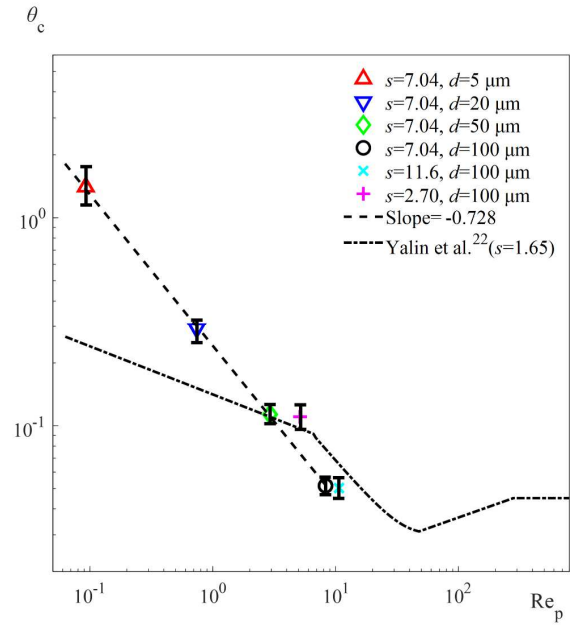
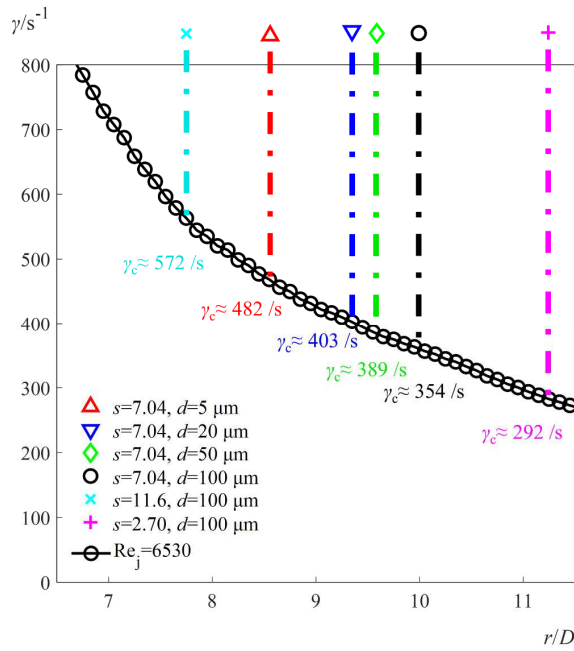
300
 301 To model the relation between particle properties and critical Shields numbers, Cao et al. [21]
 302 defined the particle Reynolds number $\text{Re}_p \equiv d\sqrt{sgd}/v$ and reported that the critical Shields

303 number θ_c was negatively correlated with the particle Reynolds number when $Re_p < 65$, based
304 on the research results of Yalin et al. [22].

305 According to our experimental results in Fig. 7, the critical shear strain rates of particles are
306 estimated in Fig. 8a. Then, the correlation between the particle Reynolds number and the critical
307 Shields number with $Re_p \in [0.093, 10.7]$ in log-log coordinates (base 10) is shown in Fig. 8b.
308 For stainless-steel particles, there is a decrease in the critical Shields number as the particle
309 Reynolds number increases, and the correlation can be described as follows, with $R^2 = 0.998$.

$$310 \quad \theta_c = 0.242 Re_p^{-0.728} \quad (8)$$

311 The slope of -0.728 we obtained is different from the slope of -0.2306 reported by Yalin et al.
312 [22] in log-log coordinates. Given that Yalin et al. has focused on sand ($s = 1.65$), this deviation
313 may be due to the high densities of stainless-steel particles. Furthermore, we observe that the
314 critical Shields numbers of low-density particles ($s = 2.7$) are close to the Shields curve for sand
315 reported by Yalin et al. [22]. Besides, with the increase of Re_p , the critical Shields numbers of
316 particles are gradually approaching 0.05, in agreement with the findings of research [20-22].



317

318

(a)

(b)

319 **Fig. 8.** (a) Estimated values of critical shear strain rates for different particles. (b) Correlation
 320 between particle Reynolds numbers and critical Shields numbers. ($Re_j = 6530$, $\delta = 0.0003$ m)

321

322 4.4 Effect of bed thickness.

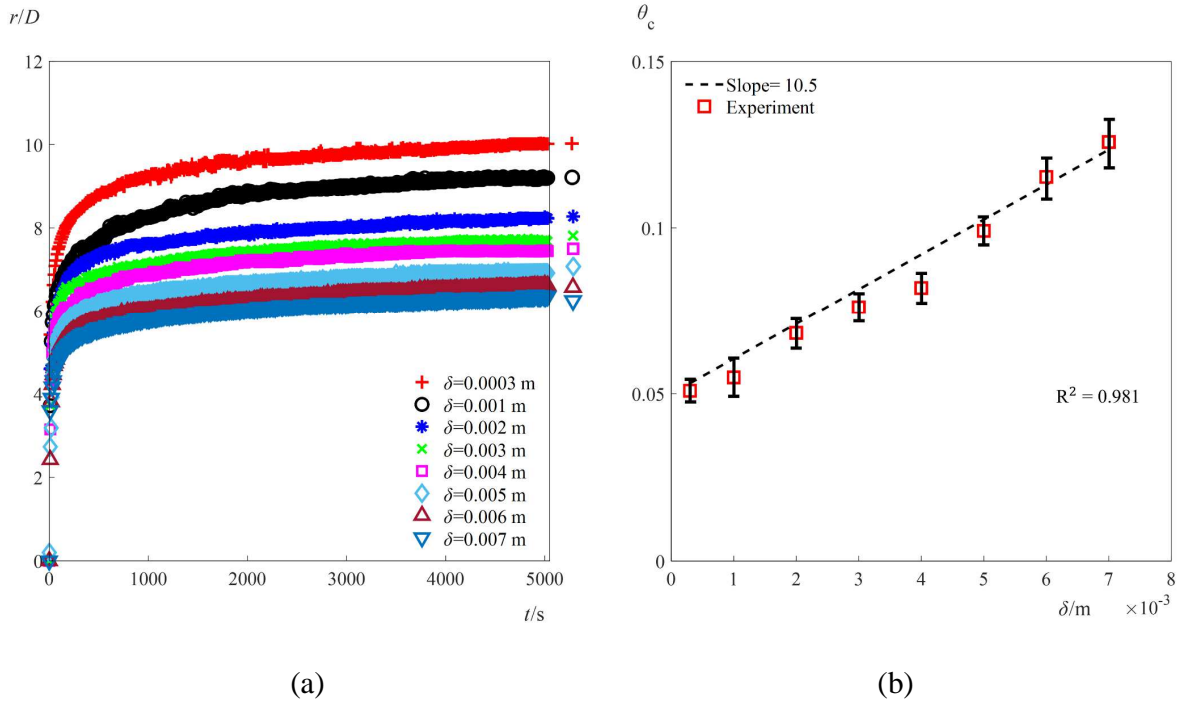
323 The temporal evolutions of bed removal radii at different bed thicknesses in our experiments
 324 are given in Fig. 9a. It is obvious that the critical removal radius of bed is negatively correlated
 325 with the bed thickness, and it takes less time to reach a stable state for a thicker bed.

326 The critical Shields numbers are collected at different bed thicknesses, see Fig. 9b. The critical
 327 Shields number for the "near zero thickness" case is about 0.05, which is in good agreement with
 328 data from published studies [20-22]. A linear correlation between the critical Shields number and
 329 the bed thickness can be described as follows, with $R^2 = 0.981$ and δ in meter.

330

$$\theta_c = 10.5 \delta + 0.05 \quad (9)$$

331



332

333

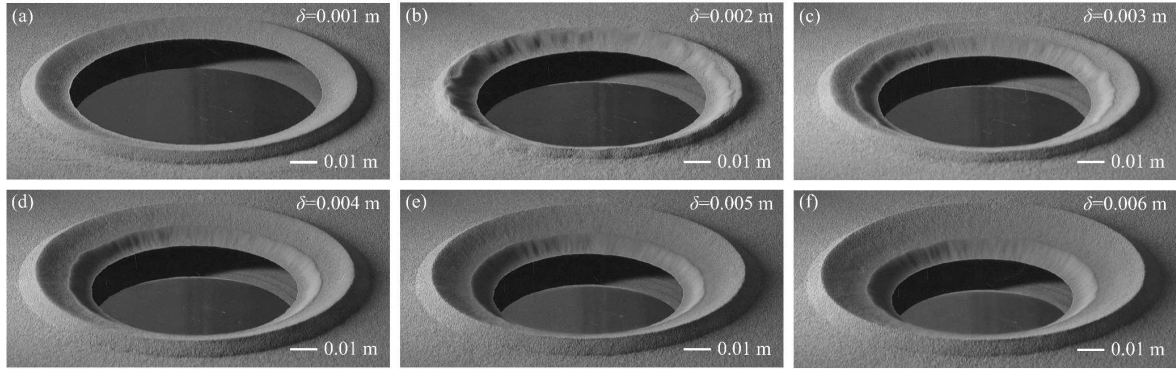
334 **Fig. 9.** (a) Bed removal radii as a function of time at different bed thicknesses. (b) Correlation
335 between critical Shields numbers and bed thicknesses. ($Re_j = 6530$, $s = 7.04$, $d = 100 \mu\text{m}$)

336

337 In Fig. 9b, a slight deviation from the fitted line can be seen around $\delta = 0.004$ m. To figure out
338 the reason for this deviation, we display stable bed patterns for different bed thicknesses in Fig.
339 10. The circular bed formed by the jet, called as "dune", is very smooth when $\delta = 0.001$ m. The
340 peak boundary of the dune become fuzzy at $\delta = 0.002$ m, accompanied by a reduction in its
341 diameter, because a second dune is forming. A pair of dunes can be clearly seen for the case of δ
342 = 0.003 m. After δ reaches 0.004 m, the two peak boundaries of the two dunes become quite
343 clear. With increasing δ from 0.004 to 0.006 m, the diameter of the peak boundary of the outer
344 dune is almost constant, but the diameter of the base boundary of the inner dune quickly

345 decreases from $15D$ to $13D$. Therefore, we consider the deviation in Fig. 9b is due to the
346 dynamic generation process of the inner dune.

347



348

349 **Fig. 10.** Stable bed patterns at bed thickness of (a) 0.001 m; (b) 0.002 m; (c) 0.003 m; (d) 0.004
350 m; (e) 0.005 m; (f) 0.006 m. ($Re_j = 6530$, $s = 7.04$, $d = 100 \mu\text{m}$)

351

352 **4.5 Bed load transport rate.**

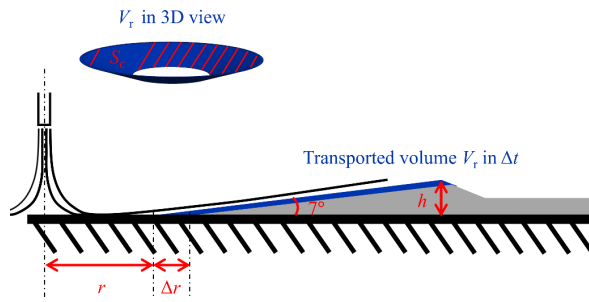
353 In shear flows, the transported bed on a horizontal surface consists of two main parts: the bed
354 load (particles moving by rolling, sliding, or in short jumps) and the suspended load (particles
355 entrained in the flow closely above the bed) [23]. According to the review of Nielsen [24], even
356 under high shear conditions ($\theta \approx 1$), the proportion of suspended load transport in the total
357 sediment transport is not more than 20%. Based on our visual observations, almost all particles
358 in this study moved as bed load when $\delta = 0.0003$ m, and only cases with initial bed thicknesses
359 of 0.0003 m are included in this section.

360 Fig. 11 shows a schematic diagram of the bed load transport, and the transported bed during
361 unit time Δt is marked in blue. When r/D is in the range [3, 8] and initial bed thickness δ is
362 0.0003 m, our experimental results show that the inner stacking angle of the dune in jet flows is

363 about 7° , and the bed stacking height h is approximately equal to 0.001 m. Then the transported
 364 volume V_r can be estimated based on the change of removal radius Δr per unit time Δt and the
 365 lateral surface area S_c of the frustum of cone. And the mass transport rate q_m of bed load per unit
 366 width at characteristic radius $r + \Delta r/2$ is calculated by dividing the transported mass by the
 367 characteristic perimeter. The calculation equation is as follows:

$$368 \quad q_m = \rho_b \frac{V_r}{\Delta t \times 2\pi(r + \Delta r/2)} \approx \rho_b \frac{\Delta r \times \sin(7^\circ) \times S_c}{\Delta t \times 2\pi(r + \Delta r/2)} = \rho_b \frac{\Delta r \times \sin(7^\circ) \times \pi \frac{h}{\sin(7^\circ)} (r + (r + \frac{h}{\tan(7^\circ)}))}{\Delta t \times 2\pi(r + \Delta r/2)} \quad (11)$$

369 where ρ_b is the packing density of bed and be known as $0.63\rho_s$ according to the random close
 370 packing [25], and $\Delta t = 1$ s is the sampling interval of the camera in this section.



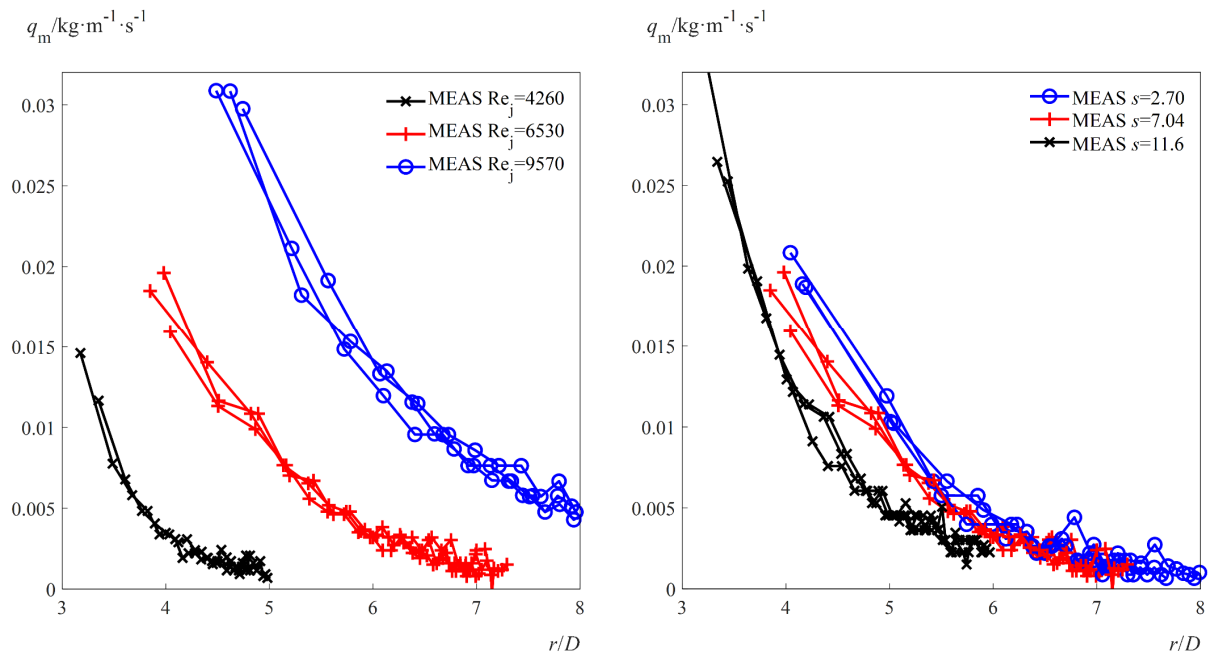
371
 372 **Fig. 11.** Schematic diagram of bed load transport in an impinging jet on a horizontal surface.
 373 (The bed and jet are scaled non-proportionally.)

374
 375 The measured bed load transport rates q_m are shown in Fig. 12. Each set of data contains the
 376 results of three repeated experiments, and they are presented with the same mark. Because the
 377 bed removal process was random and rapid (took only 1 to 2 seconds) during the interval when
 378 r/D increased from 0 to 3, we collected data starting from the location $r/D = 3$.

379 For all the cases in Fig. 12, the transport rates decline with the increase of r/D ranging from 3
 380 to 8. Fig. 12a shows that the jet Reynolds number has significant effect on the transport rate. For

381 example, q_m with Reynolds number of 4260 and 9570 at $r/D=5$ is 0.001 and 0.024 $\text{kg}\cdot\text{m}^{-1}\cdot\text{s}^{-1}$,
 382 respectively. This indicates that the particle motion exhibits a sensitive response to the increase
 383 in agitating power resulting from enhanced jet intensity. The curves resembling Fig. 6d suggest a
 384 correlation between transport rate and shear stress. The effect of particle density is shown in Fig.
 385 12b, and particles with lower density are transported at a higher rate at the same location.
 386 Compared with the first two factors, the particle diameter has a limited effect on the mass
 387 transport rate.

388

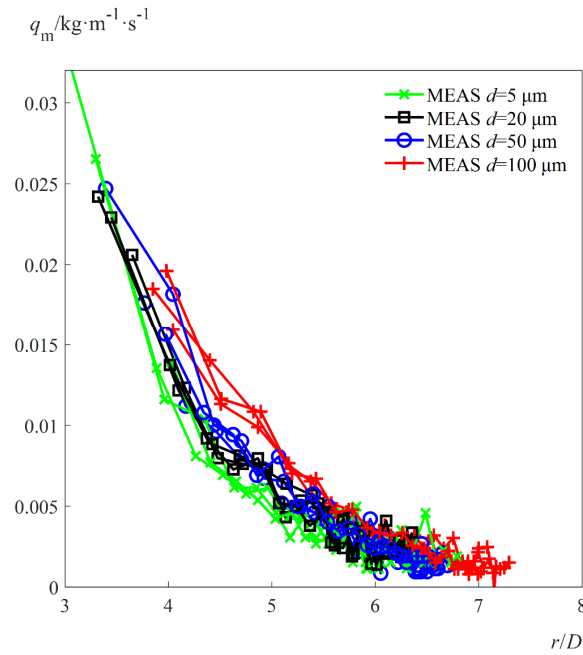


389

390

(a)

(b)



(c)

391

392

393 **Fig. 12.** Measured bed load transport rates for different (a) jet intensity; (b) particle density; (c)
 394 particle diameter. (Default values without mention: $Re_j = 6530$, $s = 7.04$, $d = 100 \mu\text{m}$, $\delta =$
 395 0.0003 m)

396

397 To our knowledge, no model for particle transport rates in vertical wall jets has been reported
 398 in the literature. We have therefore drawn inspiration from models for particle transport in river
 399 channels [26-28], specifically the one reported by Kleinhans et al. [29] for initial transport along
 400 coastlines. Our experimental data guided the necessary adaptations to this model.

401 For the prediction of bed load transport on a horizontal surface, many empirical models [26-29]
 402 were developed, and the general equation of the mass transport rate per unit of width can be
 403 written as follows:

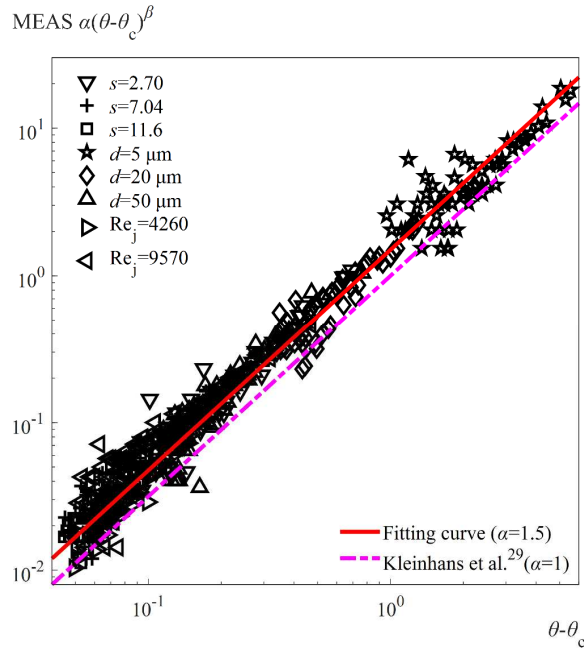
404
$$q_m = \begin{cases} \alpha(\theta - \theta_c)^\beta \times \rho_s d \sqrt{\frac{\rho_s - \rho}{\rho} g d}, & \theta \geq \theta_c \\ 0 & , \theta < \theta_c \end{cases} \quad (12)$$

405 where α and β are empirical dimensionless constants. For similar particle motion starting from
 406 rest in this study, Kleinhans et al. [29] have reported one correlation for the incipient motion of
 407 particles on the coastline, with $\alpha = 1$ and $\beta = 1.5$.

408 The measured dimensionless transport rates $\frac{q_m}{\rho_s d \sqrt{(\rho_s - \rho) g d / \rho}}$ (denoted as MEAS $\alpha(\theta - \theta_c)^\beta$) in
 409 our experiments as a function of $(\theta - \theta_c)$ are shown in Fig. 13. We consider the coefficient β as
 410 1.5, following most existing models [26-29], and then a fitted value of 1.5 is obtained for α , with
 411 $R^2 = 0.963$. A revised model is proposed as follows:

412
$$q_m = \begin{cases} 1.5(\theta - \theta_c)^{1.5} \times \rho_s d \sqrt{\frac{\rho_s - \rho}{\rho} g d}, & \theta \geq \theta_c \\ 0 & , \theta < \theta_c \end{cases} \quad (13)$$

413



414

415 **Fig. 13.** Correlation between measured dimensionless transport rates $\alpha(\theta - \theta_c)^\beta$ and $\theta - \theta_c$.
416 (Default values without mention: $Re_j = 6530$, $s = 7.04$, $d = 100 \mu\text{m}$, $\delta = 0.0003 \text{ m}$)

417

418 **5. Conclusion**

419 We studied the removal processes of horizontal beds, consisting of micron-sized spherical
420 metal particles, driven by vertical submerged water jets. Various factors such as jet intensity,
421 particle density, particle diameter, and bed thickness were considered, and single-phase large
422 eddy simulations were used to predict the shear stress acting on particles. The main conclusions
423 are summarized as follows:

- 424 1. The critical Shields number was found to be intricately related to properties of particles, and
425 independent of jet intensity. As particle Reynolds number increased, we observed that the
426 critical Shields numbers of particles gradually approached 0.05, which was consistent with
427 the published results on sediment transport. A new Shields number curve for stainless-steel
428 particles with diameter $d \leq 100 \mu\text{m}$ is proposed.
- 429 2. To verify the simulations, the velocity profiles measured using the PIV technique and the
430 wall shear stain rate profiles measured using the electrochemical diffusion technique were
431 cited. The simulated results matched well with the experimental data reported in the
432 literature.
- 433 3. Based on the bed load transport models and our experiment results, we proposed a revised
434 transport rate model. With the simulated wall shear stress profiles, the revised model could
435 accurately predict the bed load transport rates of the thin beds under the impinging jet.

436 This research could be extended in at least two ways: studying the bed motion under the jet
437 with incident angles, and carrying out larger scale experiments. They aim at the prediction of

438 transport in side-entry jets and larger containers. The numerical simulations of solid-liquid two-
439 phase flow, as well as hybrid LES and RANS approach, will be our future research directions.
440 The experimental results in this study can also provide reference for numerical model validation.
441

442 **Corresponding Authors**

443 ***Zhipeng Li** – State Key Laboratory of Chemical Resource Engineering, School of Chemical
444 Engineering, Beijing University of Chemical Technology, Beijing 100029, China;
445 orcid.org/0000-0003-1450-8836; Email: lizp@mail.buct.edu.cn

446 ***Zhengming Gao** – State Key Laboratory of Chemical Resource Engineering, School of
447 Chemical Engineering, Beijing University of Chemical Technology, Beijing 100029, China;
448 Email: gaozm@mail.buct.edu.cn

449 **Authors**

450 **Han Peng** – State Key Laboratory of Chemical Resource Engineering, School of Chemical
451 Engineering, Beijing University of Chemical Technology, Beijing 100029, China;
452 orcid.org/0000-0002-3122-8038

453 **Xinliang Jia** – China Nuclear Power Engineering Co., Ltd., Beijing 100840, China

454 **Xiaofang Guo** – China Nuclear Power Engineering Co., Ltd., Beijing 100840, China

455 **Yubo Jiang** – China Nuclear Power Engineering Co., Ltd., Beijing 100840, China

456 **J. J. Derksen** – School of Engineering, University of Aberdeen, Aberdeen AB24 3UE, U.K.;
457 orcid.org/0000-0002-9813-356X

458

459 **CRedit Authorship Contribution Statement**

460 **Han Peng:** Writing – original draft. **Xinliang Jia:** Software. **Xiaofang Guo:** Methodology.

461 **Yubo Jiang:** Resources. **Zhipeng Li:** Writing – review & editing. **Zhengming Gao:** Supervision.

462 **J. J. Derksen:** Writing – review & editing.

463

464 **Declaration of Competing Interes**

465 The authors declare no known competing financial interest.

466

467 **Acknowledgments**

468 This research did not receive any specific grant from funding agencies in the public,

469 commercial, or not-for-profit sectors.

470

471 **Supplementary Material**

472 Independence test results of grid size and CFL number can be found in the supplementary data.

473

474 **NOMENCLATURE**

C_w	a coefficient in the simulation, -
D, D_o	inner and outer diameter of nozzle outlet, m
d	average particle diameter, μm
g	gravitational acceleration, $\text{m}\cdot\text{s}^{-2}$
H	liquid height in the square glass tank, m
h	stacking height of bed, m

L	side length of the square glass tank, m
p	the pressure in the simulation, $\text{N}\cdot\text{m}^{-2}$
q_m	mass transport rate of bed load per unit width, $\text{kg}\cdot\text{m}^{-1}\cdot\text{s}^{-1}$
Re_j	jet Reynolds number, $Re_j \equiv \rho Du/\mu$, -
Re_p	particle Reynolds number, $Re_p \equiv d\sqrt{sgd}/v$, -
r	radius of the lower edge of the impact pit, m
S_c	lateral surface area of the frustum of cone, m^2
S_{ij}	deformation tensor of the resolved field in the simulation, s^{-1}
S_{ij}^d	traceless symmetric part of the square of the velocity gradient tensor, s^{-2}
s	submerged specific weight of sediment, $s = \rho_s/\rho - 1$, -
t	duration of jet, s
U_f, U_r	frictional velocity and flow velocity around particles, $\text{m}\cdot\text{s}^{-1}$
u_0	mean flow velocity within the tube, $\text{m}\cdot\text{s}^{-1}$
u_i, u_j	the velocity component in different coordinate directions in the simulation, $\text{m}\cdot\text{s}^{-1}$
u_r, u_x	transverse velocity, $\text{m}\cdot\text{s}^{-1}$
u_z	streamwise velocity, $\text{m}\cdot\text{s}^{-1}$
V	volume of a computational cell, m^3
V_r	transported volume in unit time, m^3
y	distance to the closest wall, m
y^+	dimensionless distance to the closest wall, $y^+ \equiv \rho y U_f/\mu$, -

475

476 **Greek letters**

α, β	empirical constant for the bed load transport model, -
γ, γ_c	shear strain rate and critical shear strain rate, s^{-1}
δ	initial bed thickness, m
Δ	filter width in the simulation, m
Δr	change of the removal radii, m

Δt	time step or interval, s
Δx_{\max}	maximum grid spacing in the simulation, m
θ, θ_c	Shields number and critical Shields number, $\theta \equiv \tau / (g(\rho_s - \rho)d)$, -
κ	von Karman constant, -
μ	dynamic viscosity of water, $\text{N} \cdot \text{s} \cdot \text{m}^{-2}$
ν, ν_t	kinematic viscosity of the liquid and the eddy viscosity, $\text{m}^2 \cdot \text{s}^{-1}$
ρ, ρ_b, ρ_s	density of liquid, packing density of particles, and density of particles, $\text{kg} \cdot \text{m}^{-3}$
σ	the sub-grid scale stress tensor in the simulation, $\text{N} \cdot \text{m}^{-2}$
τ, τ_c	shear stress and critical shear stress, $\text{N} \cdot \text{m}^{-2}$

477

478 **Abbreviations**

j	jet
MEAS	measured values by experiments
PIV	measured values by using particle image velocimetry
p	particle
SIM	simulated values
s	sediment

479

480 **References**

- 481 [1] P. C Upson, Highly active liquid waste management at sellafield. *Prog. Nucl. Energ.* 13(1)
482 (1984) 31-47.
- 483 [2] R. Natarajan, Reprocessing of spent nuclear fuel in India: present challenges and future
484 programme. *Prog. Nucl. Energ.* 101 (2017) 118-132.
- 485 [3] P. K. Wattal, Back end of indian nuclear fuel cycle-a road to sustainability. *Prog. Nucl.*
486 *Energ.* 101 (2017) 133-145.

- 487 [4] A. Shields, Anwendung der Aehnlichkeitsmechanik und der Turbulenzforschung auf die
488 Geschiebebewegung. *PhD Thesis Technical University Berlin* 1936.
- 489 [5] P. A. Mantz, Incipient transport of fine grains and flakes by fluids—extended Shields
490 diagram. *Journal of the Hydraulics Division* 103(6) (1977) 601-615.
- 491 [6] R. M. Young, M. J. Hargather, G. S Settles, Shear stress and particle removal measurements
492 of a round turbulent air jet impinging normally upon a planar wall. *J. Aerosol Sci.* 62 (2013)
493 15-25.
- 494 [7] D. I. Wilson, P. Atkinson, H. Köhler, M. Mauermann, H. Stoye, K. Suddaby, T. Wang, J.F.
495 Davidson, J. P. Majschak, Cleaning of soft-solid soil layers on vertical and horizontal
496 surfaces by stationary coherent impinging liquid jets. *Chem. Eng. Sci.* 109 (2014) 183-196.
- 497 [8] H. Wang, Z. Yang, B. Li, S. Wang, Predicting the near-wall velocity of wall turbulence using
498 a neural network for particle image velocimetry. *Phys. Fluids* 32(11) (2020) 115105.
- 499 [9] D. J. Phares, G. T. Smedley, R. C Flagan, The wall shear stress produced by the normal
500 impingement of a jet on a flat surface. *J. Fluid Mech.* 418 (2000) 351-375.
- 501 [10] M. Kristiawan, K. Sodjavi, B. Montagné, A. Meslem, V. Sobolik, Mass transfer and shear
502 rate on a wall normal to an impinging circular jet. *Chem. Eng. Sci.* 132 (2015) 32-45.
- 503 [11] M. El Hassan, H. H. Assoum, R. Martinuzzi, V. Sobolik, K. Abed-Meraim, A. Sakout,
504 Experimental investigation of the wall shear stress in a circular impinging jet. *Phys. Fluids*
505 25(7) (2013) 077101.
- 506 [12] K. Sodjavi, B. Montagné, P. Bragança, A. Meslem, P. Byrne, C. Degouet, V. Sobolik, PIV
507 and electrodiffusion diagnostics of flow field, wall shear stress and mass transfer beneath
508 three round submerged impinging jets. *Exp. Therm. Fluid Sci.* 70 (2016) 417-436.
- 509 [13] A. D. Eisner, The impact of the surface macro-roughness on the surface shear stress and rate
510 under the oblique linear cylindrical nozzle jet as pertinent to particles detachment. *J.*
511 *Aerosol Sci.* 102 (2016) 16-28.

- 512 [14] F. Nicoud,; F. Ducros, Subgrid-scale stress modelling based on the square of the velocity
513 gradient tensor. *Flow Turbul. Combust.* 62(3) (1999) 183-200.
- 514 [15] A Fluent, Ansys Fluent Theory Guide. ANSYS Inc. 2021, USA, pp.116-129.
- 515 [16] T. J. Atherton, D. J. Kerbyson, Size invariant circle detection. *Image Vision Comput.* 17(11)
516 (1999) 795-803.
- 517 [17] J. J. Derksen, Simulations of granular bed erosion due to a mildly turbulent shear flow. *J.*
518 *Hydraul. Res.* 53(5) (2015) 622-632.
- 519 [18] A. Meslem, V. Sobolik, F. Bode, K. Sodjavi, Y. Zaouali, I. Nastase, C. Croitoru, Flow
520 dynamics and mass transfer in impinging circular jet at low Reynolds number. Comparison
521 of convergent and orifice nozzles. *Int. J. Heat Mass Tran.* 67 (2013) 25-45.
- 522 [19] M. J. Tummers, J. Jacobse, S. G. Voorbrood, Turbulent flow in the near field of a round
523 impinging jet. *Int. J. Heat Mass Tran.* 54(23-24) (2011) 4939-4948.
- 524 [20] J. Fredsøe, R. Deigaard, Mechanics of Coastal Sediment Transport. *World Scientific.* 1992.
525 pp.201-205.
- 526 [21] Z. Cao, G. Pender, J. Meng, Explicit formulation of the Shields diagram for incipient
527 motion of sediment. *J. Hydraul. Eng.* 132(10) (2006) 1097-1099.
- 528 [22] M. S. Yalin, A. F. Da Silva, Fluvial processes. *IAHR monograph.* 2001. IAHR, Delft, The
529 Netherlands.
- 530 [23] F. Engelund, J. Fredsøe, A sediment transport model for straight alluvial channels.
531 *Hydrology Research* 7(5) (1976) 293-306.
- 532 [24] P. Nielsen, Coastal bottom boundary layers and sediment transport. *World Scientific.* 1992.
533 pp.109-115.
- 534 [25] R. A. Bagnold, The flow of cohesionless grains in fluids. *Philosophical Transactions of the*
535 *Royal Society of London. Series A, Mathematical and Physical Sciences.* 249(964) (1956)
536 235-297.

- 537 [26] E. Meyer-Peter, R. Mueller, Formulas for bed-load transport. Proceedings 2nd meeting. Int.
538 Ass. for Hydraulic Structures Res. 1948. Stockholm, Sweden, pp. 39–64.
- 539 [27] R. Fernandez Luque, R. Van Beek, Erosion and transport of bed-load sediment. *J. Hydraul.*
540 *Res.* 14(2) (1976) 127-144.
- 541 [28] P. L. Wiberg, J. Dungan Smith, Model for calculating bed load transport of sediment. *J.*
542 *Hydraul. Eng.* 115(1) (1989) 101-123.
- 543 [29] M. G. Kleinhans, B. T. Grasmeijer, Bed load transport on the shoreface by currents and
544 waves. *Coast. Eng.* 53(12) (2006) 983-996.